Space weather effects on midlatitude HF propagation paths: Observations and a data-driven *D* region model

J. V. Eccles

Space Environment Corporation, Providence, Utah, USA

R. D. Hunsucker

RP Consultants, Klamath Falls, Oregon, USA

D. Rice and J. J. Sojka

Space Environment Corporation, Providence, Utah, USA

[1] A two-pronged study is under way to improve understanding of the *D* region response to space weather and its effects on HF propagation. One part, the HF Investigation of *D* region Ionospheric Variation Experiment (HIDIVE), is designed to obtain simultaneous, quantitative propagation and absorption data from an HF signal monitoring network along with solar X-ray flux from the NOAA GOES satellites. Observations have been made continuously since late December 2002 and include the severe disturbances of October–November 2003. GOES satellite X-ray observations and geophysical indices are assimilated into the Data-Driven *D* Region (DDDR) electron density model developed as the second part of thisproject. ACE satellite proton observations, the HIDIVE HF observations, and possibly other real-time space weather data will be assimilated into DDDR in the future. Together with the Ionospheric Forecast Model developed by the Space Environment Corporation, DDDR will provide improved specification of HF propagation and absorption characteristics when supplemented by near-real-time propagation observations from HIDIVE.

1. Introduction

[2] Most midlatitude ionospheric models and HF propagation prediction programs include the solar zenith angle and the frequency-squared variation of absorption, but the increased *D* region absorption caused by specific space weather effects such as solar X-ray events is not included. The purpose of the HF Investigation of *D* region Ionospheric Variation Experiment (HIDIVE) and Data-Driven *D* Region (DDDR) programs is to obtain pertinent absorption data and assimilate them to produce improved *D* region absorption model and HF propagation prediction programs. The Data-Driven *D* Region model described here is combined with an *E* and *F* region model [*Schunk et al.*, 1997] for propagation and absorption studies. The impact of space weather on the midlatitude ionosphere is demonstrated by the effects of the extreme solar events of October–November 2003 on a typical midlatitude HF propagation path. Fadeouts are even more pronounced at high latitudes [*Hunsucker and Hargreaves*, 2003]. This is timely because of renewed interest in the use of HF circuits by the military and civil defense [*Cook*, 1997; *Renfree*, 2001; *Bishop et al.*, 2004] and commercial users [*Goodman*, 1992; *Lanzerotti*, 2001; *Hunsucker and Hargreaves*, 2003; *Murtagh et al.*, 2004].

[3] Monitoring of standard time-frequency HF stations has been employed for the past three decades and some examples are discussed by *Davies* [1990, pp. 213, 347], *McNamara* [1991, pp. 95–96], *Croft* [1972], *Bixby* [1956] and *American Radio Relay League* [2003, pp. 23–26, 23–45]. Since *active* methods for studying HF propagation were introduced in 1925 (see the discussion in chapter 2 of *Hunsucker* [1991]) the *passive* monitoring technique was mainly applied for studies of the high-latitude and equatorial ionosphere, thus long-term, quantitative data on the midlatitude ionosphere are difficult to find in archival literature. Recently, (K. Davies, personal communication, 2004) reported that there was a program of aural measurements of WWV signal strength at ionospheric stations in Canada in the late 1940s and 1950s which illustrated the diurnal patterns of propagation from 2.5 to 25 MHz. These data, however, were not published.

[4] The unique contribution of the present study is the simultaneous measurement of digitized, calibrated HF signal amplitude on several paths once per minute over the declining phase of sunspot cycle 23, while modeling the ionospheric conditions along these paths. Comparison of the theoretical and observational data sets will allow assessment of the model's performance and of the impact

Figure 1. Map of HIDIVE monitoring sites and the propagation paths from the WWV and WWVH transmitters.

of unmodeled ionospheric phenomena such as sporadic *E* and atmospheric waves. Assimilation of the observations into the DDDR model should allow for corrections to be made and notifications of unusual conditions to be issued to users in near real time. The archived data sets will be useful for various comparative studies of space weather effects on propagation and other ionospheric models in the near future.

2. Experimental Technique

[5] To obtain *D* region absorption data we have deployed three HF receivers to continuously record signal amplitude from the U.S. standard time stations WWV located in Fort Collins, Colorado, and WWVH in Kekaha, Kauai, Hawaii. The midlatitude paths are shown in

Figure 1. WWV and WWVH use very stable transmitters and nondirectional antennas at 10.0 kW levels on 5.0, 10.0 and 15.0 MHz and on 2.5 MHz at 2.5 kW (WWV) and 5 kW (WWVH); WWV alone transmits simultaneously on 20.0 MHz at 2.5 kW. The HIDIVE monitors are located in Klamath Falls (KF), Oregon; Providence (PRV), Utah; and Bear Lake Observatory (BLO), Utah (Table 1). Another monitoring system operated by the Air Force Research Laboratory at Hanscom AFB in Massachusetts has also contributed to this study.

[6] HIDIVE HF monitoring stations are relatively low cost (about US$ 2000 each) systems consisting of computer-controlled receivers fed by wideband HF antennas as shown in Figure 2. Barker and Williamson terminated folded dipole antennas are used at Klamath Falls and Bear Lake Observatory, while a smaller shortwave listening

Table 1. HIDIVE Monitoring Locations and Great Circle Path Distances to Transmitters

Monitor	Location	Latitude, deg. N	Longitude, deg. W	WWV Path, km	WWVH Path, km
BLO	Garden City, Utah	41.934	111.421	550	4990
PRV	Providence, Utah	41.712	111.830	579	4951
KF	Klamath Falls, Oregon	42.173	121.850	1409	4167
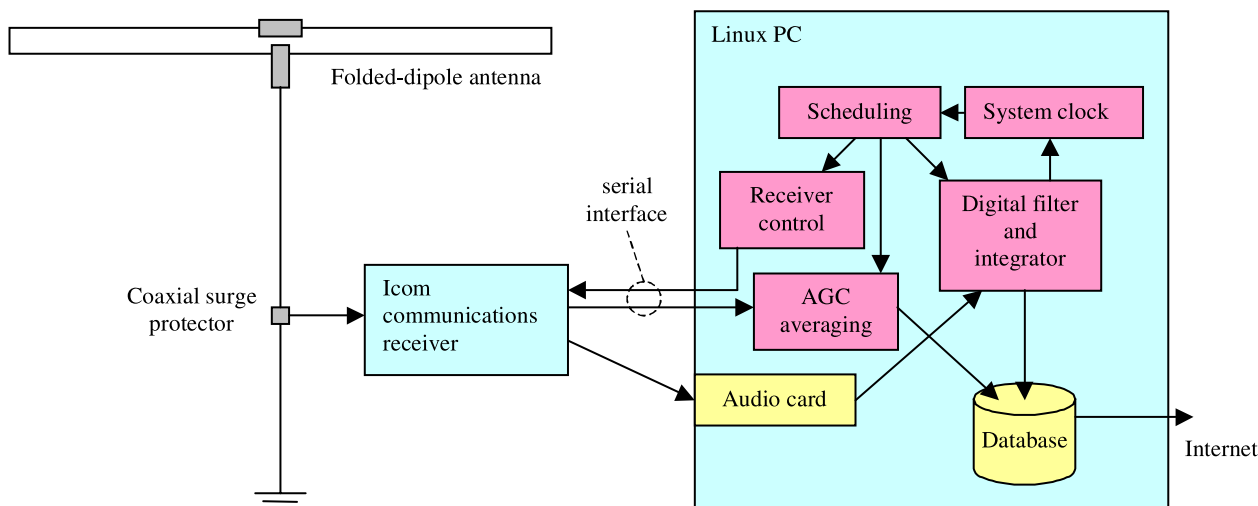
Figure 2. HF monitoring system block diagram. Digital filtering is used to separate WWV and WWVH signals and also provides time synchronization for the system clock.

trapped dipole is used for the Providence system (Table 2). The receivers are Icom HF communications receivers enhanced with temperature-stabilized crystal oscillators. Each receiver is equipped with a serial interface which allows almost all radio settings to be controlled using a proprietary command set. Software was developed to allow a Linux PC to control receiver frequency, mode, and other parameters according to an hourly schedule.

[7] The BLO and KF monitors are regarded as primary sites. The Space Environment Corporation (SEC) site in Providence, Utah, is the development site where software modifications are tested. Note that the original development system was moved from SEC to BLO in November 2003, and a different receiver was installed at SEC; to avoid confusing the data sets, the Providence site is designated PRV following the equipment change. The Providence site does not have sufficient real estate to set up a full-sized terminated folded dipole, so a smaller trapped dipole was installed at this site. While this antenna was not intended for serious data collection, the data collected by the Providence development system has proven useful for many of the analyses performed thus far.

[8] The serial interface also allows the PC to read the receiver's automatic gain control (AGC) level, which provides a logarithmic measure of the received signal strength. This value reflects the RF gain which is automatically adjusted by a closed-loop control system in the receiver to maintain a constant audio level as the RF signal level fluctuates. In many monitoring systems, the AGC level alone provides the received signal strength value, but unfortunately the AGC level does not provide any indication of the quality of the received signal. For example, a high AGC level could be produced by strong local interference when the desired signal is completely absent.

[9] To avoid this problem, the monitoring system also digitizes the receiver audio signal and uses digital filtering to analyze the audio frequencies received. WWV and WWVH broadcast specific tones (usually 500 and 600 Hz, though others are used at particular times) as part of the 1-s tick pattern. The two stations use different tone schedules, so for a given second WWV may be transmitting 500 Hz while WWVH transmits 600 Hz. The monitoring software uses the published tone schedule to determine the relative strength of the WWV and WWVH transmissions. Comparing the adjacent audio frequencies (e.g., 400 and 700 Hz) and the overall audio signal level allows the WWV/WWVH transmissions to be distinguished from interfering signals or noise. The timing of the tone pulses is also used to keep the monitoring PCs synchronized to within half a second of universal time.

[10] The monitoring software integrates audio signal levels and AGC levels over 1-min intervals. There are periods in which no tones are transmitted while voice bulletins are broadcast (weather, geomagnetic conditions, station identification, and so forth) and no signal data are taken during these periods.

[11] Audio and AGC signal levels have been calibrated against a signal generator at each operating frequency;

Table 2. HIDIVE Monitoring Configurations

Monitor	Start Date	Receiver	Antenna	Antenna Configuration
KF	31 Dec. 2002	Icom IC-R75	90' term folded dipole	Inverted V, 39' apex
SEC	19 Dec. 2002	Icom IC-R75	42' trapped dipole	Inverted V, 15' apex
PRV	12 Nov. 2003	Icom IC-718	42' trapped dipole	Inverted V, 15' apex
BLO	19 Nov. 2003	Icom IC-R75	90' term folded dipole	Flat, 20' height
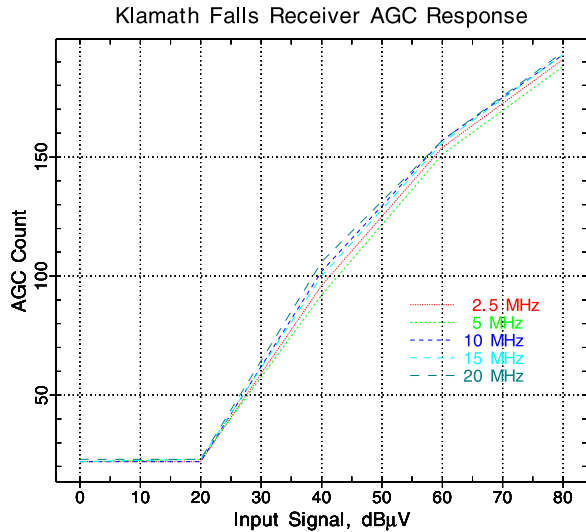
Figure 3a. AGC calibration for KF receiver. AGC is not active for weak signals (<20 dB μV), and audio signal strength reflects the RF signal strength in that region. AGC response is consistent over the frequency range of interest, with values varying by a few counts for a given signal level.
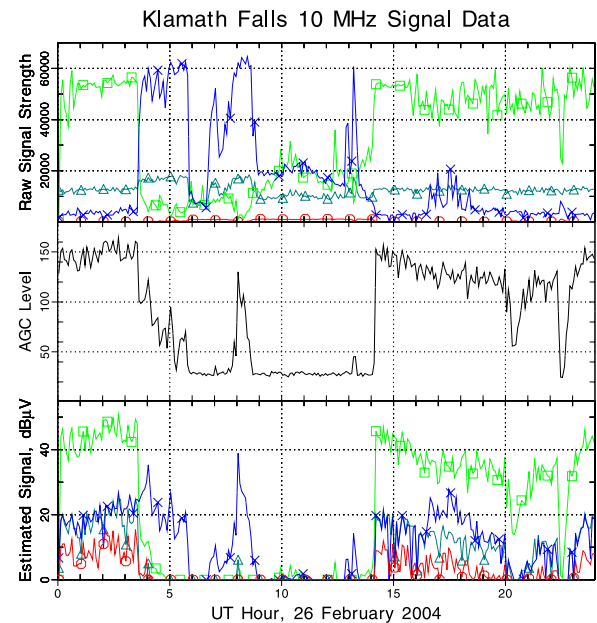
the audio spectrum broadening prevents a signal less than about 25 dB below the stronger signal from being detected. For example, in Figure 3b from 0000–0330 UT, the WWV signal is about ~45 dB μV, while the WWVH signal *appears* to be ~20 dB μV. However, closer examination shows that the WWVH signal is following the WWV audio sideband level, so we can only state that the WWVH signal is ≤20 dB μV during this period. On the other hand, the WWVH signal enhancement around 0800 UT rises 30 dB above its audio sidebands, indicating less ionospheric distortion than in the earlier case. The signature of this enhancement suggests that it is likely due to a low-angle sporadic *E* path and thus exposed to less ionospheric spectral broadening than the earlier WWV signal would experience along its probable *F* region path. The potential relationship between spectral broadening and ionospheric path requires further investigation.

[14] Signal amplitude data from WWV/WWVH have been recorded since December 2002 and we plan to continue measurements through June 2005. SEC supplements the HF signal amplitude observations with magnetometer and ionosonde data from its instruments at Bear Lake Observatory in Utah, which is located near the midpoint of the WWV to Klamath Falls path. SEC also collects the solar X-ray flux data from the NOAA GOES

calibration curves for the Klamath Falls (KF) receiver are shown in Figure 3a. A signal level of 0 dB μV corresponds to an RF signal with 1 μV peak-to-peak amplitude, amplitude modulated by a 1 kHz audio tone. We define dB μV as 20 log ($V_{in[peak-to-peak]}$/1 μV). At low signal levels (< 20 dB μV) the AGC is unable to control the audio level, and the audio level increases with the applied signal amplitude. As signal levels increase, AGC becomes effective and the audio level becomes essentially constant, while the AGC count increases with increasing signal amplitude as shown in Figure 3a.

[12] The tables of audio and AGC levels versus calibrated input signal are used to estimate the received signal level at the receiver antenna terminals; typical results are shown in Figure 3b. Audio levels for FFT bins of interest are calculated (top), and the receiver AGC count is read (middle). The AGC count is used to establish the maximum input signal level, and each audio frequency bin is scaled against that level to arrive at the estimated signal level (bottom). Since we are primarily interested in relative signal variations in the present study, we have not attempted to estimate the absolute signal strength at the antenna. However, as we look at more detailed comparisons between model and observation, we will include antenna directivity and losses.

[13] The dynamic range of the receiver is more than 50 dB, and can be extended with the built-in preamplifier and attenuator, though the current monitoring software does not take advantage of these features. One limitation in analysis is that the broadcast audio tone spectrum is broadened by ionospheric distortion; the tones transmitted by WWV and WWVH are typically only 100 Hz apart, so

Figure 3b. HIDIVE data processing steps. (top) The audio signal is filtered to identify various components: WWV (squares), WWVH (crosses), time code (triangles), and noise floor (circles). (middle) The AGC level is used together with calibration data to scale the audio levels into estimated signal levels (bottom). (bottom) The signal levels are shown for WWV (squares) and WWVH (crosses), with audio sideband levels to identify effective signal processing noise floor (triangles and circles).
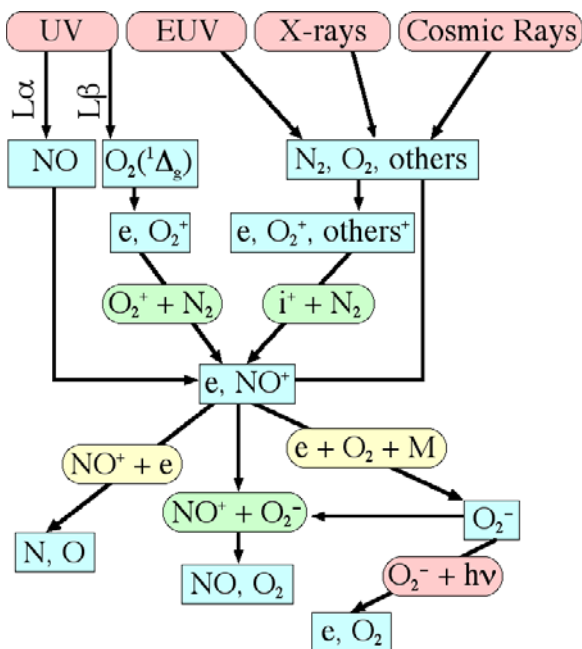
Figure 4. Ionization and subsequent ion chemistry in a mixed neutral atmosphere.

satellites, F10.7 and *Kp* values via the Internet from the Space Environment Center in Boulder, Colorado.

3. DDDR Model Description

[15] The Data-Driven *D* Region (DDDR) model is a simple ion chemistry model of the *D* region designed to incorporate sufficient positive and negative ion chemistry to generate an appropriate electron density for a wide range of natural geophysical conditions. The model must accommodate the widest of conditions: from low-density nighttimes to dramatic daytime solar flare X-ray storms and high-latitude solar proton events. The *D* region model uses data streams available at NOAA, which provide real-time input into the space weather events that affect *D* region densities. The *D* region electron profiles provided by the DDDR model are then used to calculate HF absorption characteristics for HF propagation paths. Ionosphere models of the *E* and *F* region are combined with the DDDR to provide a complete electron density specification for HF propagation and absorption estimates. The HIDIVE experiment provides a quantitative measure of *D* region HF signal attenuation to test the predictions of the model absorption calculations. Presently, the *D* region model contains sufficient physics and chemistry to provide an electron density profile from 40 to 110 kilometer altitude for midlatitude and low-latitude HF propagation paths. The current chemistry provides for the main characteristics of the electron profiles with electrons, positive and negative ions. This paper demonstrates the first results from the complete *D*, *E*, and *F* region models with full HF propagation and attenuation codes.

[16] The model *D* region assumes transport is not important. The system of time-dependent mass equations for all ion species and electrons at a location and altitude are

$$\frac{\partial n_i}{\partial t} = P_i - L_i, \tag{1}$$

where n_i is ion density, P_i is the ion production rate, and L_i is the ion loss rate. This system of equations is solved using the Livermore Solver for Ordinary Differential Equations (LSODE) [*Hindmarsh*, 1983]. The neutral species and neutral temperatures are provided by empirical neutral atmosphere models. MSIS [*Hedin*, 1991] provides the major neutral species, N_2, O_2, O, Ar, etc. The Air Force neutral atmosphere profiles within the MODTRAN model [*Anderson et al.*, 1986] provide minor species densities, N_2O, NO_2, CO_2, CO, H_2O, OH, O_3, NO, etc. The MODTRAN NO densities are not sufficient to provide for a proper *D* region model. This will be addressed in future DDDR versions. The simplified ion chemistry is represented by the species NO^+, O_2^+, O^-, O_2^-, and e to produce *E* and *D* region profiles that respond to energetic forcing from solar X rays, cosmic rays, etc. The species and reactions are defined through a setup file; thus more complex chemistry can be added to improve electron density profile fidelity. The model contains the following chemical processes: photoionization, energetic particle ionization, secondary electron ionization, ion-electron and ion-ion recombination, three-body attachment, photo-detachment, and ion-neutral chemistry.

[17] The auroral region and solar proton events have not yet been placed in the model so the DDDR remains a low-latitude and midlatitude model of the *D* region. Figure 4 diagrams the physical processes in the model with focal negative and positive ion branching represented by key O_2^- and NO^+ species. Future additions to the model will include increased ion chemistry, hydration ions, the self-consistent determination of $O_2(^1\Delta_g)$ and an improved NO density model. Metal ion chemistry is presently not envisioned.

[18] The ionization sources are divided into mechanisms and energetic regions. Cosmic ray background is applied day and night with F10.7A dependence and latitude dependence. The night sky ionization is from the geocorona and starlight sources [*Strobel et al.*, 1980] with F10.7 and solar angle dependencies. The Lyman α and Lyman β are presently F10.7 dependent as well, but sources of real time observations can be ingested. The solar flare X rays are determined by the 5-min observations from GOES 10 and GOES 12 over the integrated bands 0.05 to 0.4 nm and 0.1 to 0.8 nm. The two are combined to define an X-ray spectrum for deep atmosphere ionization. Soft X-ray energy flux from 1 to 5 nm is determined by a combination of a quiet time spectrum related to F10.7 and a flare spectrum presently related to the X rays observed by GOES. The soft X rays are critical for the daytime *D* region electron densities, but there is no real time measurement of soft X rays. The EUV spectrum is obtained from the EUVAC model [*Richards et al.*, 1994a, 1994b] relating F10.7

Providence, Utah (10/17/2003)
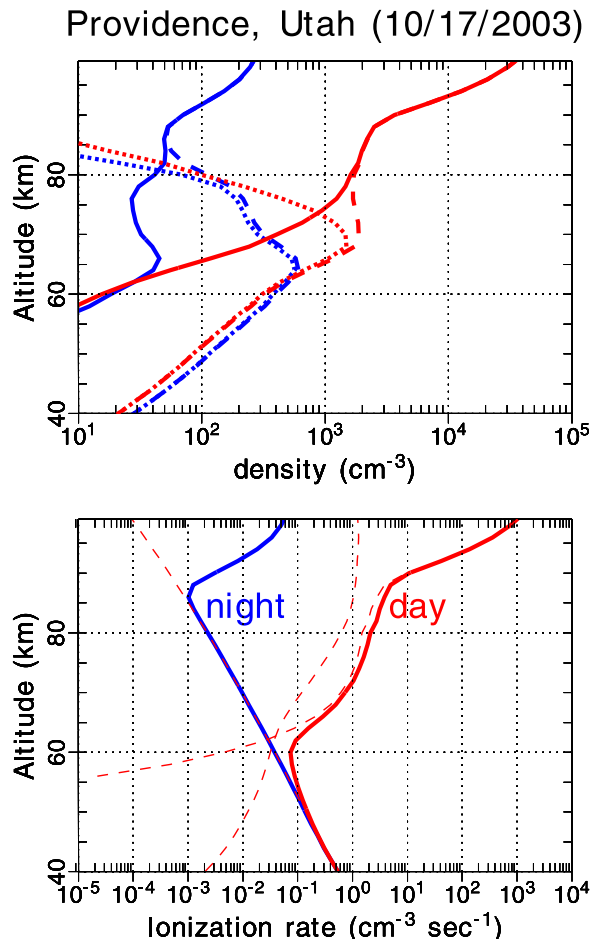
Figure 5. (top) Density profiles of negative ions (short-dashed curve), positive ions (long-dashed curve), and electrons (solid curve). (bottom) Ion-electron pair production profiles for noon (red) and midnight (blue).

and F10.7A indices to the energy flux. The ionization cross sections and absorption cross sections for the above energy spectrum are from the EUVAC model of *Richards et al.* [1994a, 1994b] with additional higher-energy bins from *Kirby et al.* [1979] and *Banks and Kockarts* [1973].

[19] The extreme range of these sources for *D* region ionization was used to test the robustness of the numerical procedures for quiet ambient conditions and disturbed conditions. Figure 5 (bottom) has the ionization profile associated with noon (red) and midnight (blue) extremes and the resulting profiles. Figure 5 (top) has density profiles for noon (red) and midnight (blue) for electrons (solid line), positive ions (long-dashed line), and negative ions (short-dashed line).

[20] The Data-Driven *D* Region electron density model is combined with the Ionospheric Forecast Model (IFM) [*Schunk et al.*, 1997] to provide *E* and *F* region densities to support ray-tracing and HF propagation codes. The IFM calculation provides electron densities from 90 to 1600 km, the DDDR model from 40 to 110 km. The two are blended between 100 and 110 km altitude.

[21] The models are run to provide a regional electron density specification every 5 to 15 min for HF ray paths from the WWV Colorado transmission site to the HIDIVE monitors in Oregon and Utah. The ray tracing code, HASEL, developed by *Coleman* [1993] is then used to determine the ray paths through the model ionosphere. The Runga-Kutta-Fehlberg numerical technique is used to solve the Haselgrove equations. The absorption calculations include full path calculations through the *D*, *E*, and *F* regions restricted to nondeviative absorption, and includes focusing effects. The HF propagation paths with absorption characteristics are calculated for 88 elevation angles in the great circle plane from the WWV transmitter to the KF HF monitor. Multiple hops of the HF path are included (currently only 2 hops). Ground-level single strength is calculated by interpolating between the individual rays. Ground-level signals from both *E* mode and *F* mode propagation with multiple hops are summed to obtain total signal strength at the monitor site. Attenuation of the signal is calculated along the ray paths on the basis of nondeviative absorption and focusing effects. The *attenuation* of radio waves can be described by,

$$E = E_o \exp(-\kappa L), \tag{2}$$

where E is field strength of attenuated wave, E_0 is field strength of unattenuated wave, κ is the absorption coefficient of medium, and L is the length of path. The absorption coefficient formula (in dB/km) is

$$\kappa = 4.6 \times 10^{-2} \left[\frac{n_e \nu_e}{\nu_e^2 + \omega_{HF}^2} \right], \tag{3}$$

where ν_e is the total electron collision frequency on neutrals and ions and ω_{HF} is the angular frequency of the transmission. This expression holds for nondeviative absorption, which is the dominant contributor to HF absorption on paths crossing the daytime *D* region [*Davies*, 1990]. Deviative absorption can be added simply, but is a only a correction to the dominant nondeviative absorption.

[22] Figure 6 shows the solar X-ray variations measured by GOES 12 and the resulting absorption coefficients at 2.5, 5, 10, 15, and 20 MHz for the *D* region above Utah, corresponding to the WWV frequencies being monitored by HIDIVE. On day 302 the flare at 2100 UT occurs during sunlight hours at Providence, Utah, and hence the absorption increases markedly. To a lesser extent, earlier on day 302 and around dawn on day 303 (1445 UT), the *D* region is responding to X-ray fluctuations. The 2100 UT day 302 flare response is most pronounced at higher frequencies where the normal daytime solar EUV absorption response is least.

4. HIDIVE-Model Comparisons

[23] The HF Investigation of *D* region Ionospheric Variation Experiment (HIDIVE) has been developed in parallel with the DDDR model to obtain simultaneous, quantitative *D* region absorption data from an HF signal –
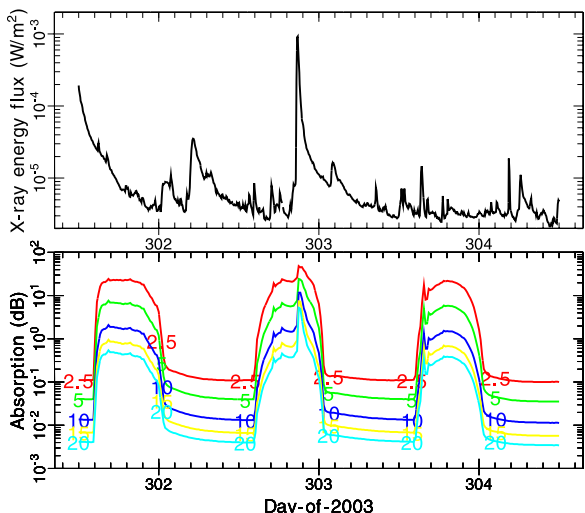
Figure 6. (top) GOES X-ray observations used within the DDDR. (bottom) HF absorption coefficient for different HF frequencies for several days in October 2003.

monitoring network. To simplify the comparison we focused on the propagation paths from WWV (Fort Collins, Colorado) to Klamath Falls, Oregon (KF) via Bear Lake Observatory, Utah (BLO.) The great circle distance is 1409 km on an azimuth of 280° from WWV to KF, and 579 km from WWV to BLO. The most probable paths from WWV to KF involve one or two hops from the *F* region; this geometry is shown in Figure 7. Note that BLO is located about 120 km from the WWV–KF path midpoint.

[24] The observed (HIDIVE) and modeled (DDDR) signal strengths for the WWV–KF path are shown in Figures 8, 9, 10, and 11 for 2.5, 5, 10, and 15 MHz, respectively. The 20 MHz WWV signal is not routinely observed in KF, and the model indicates that it is above the path maximum useable frequency (MUF) for most conditions.

4.1. Climatological Comparisons

[25] The observations and model behavior observed in Figures 8–11 generally follow seasonal and diurnal

expectations for HF propagation. These trends at each of the five frequencies are described in the following paragraphs.

4.1.1. Signal at 2.5 MHz (Figure 8)

[26] These signals (left) are strongest at night when they are easily refracted by the *F* region. During the day they are very weak due to *D* region absorption. The model follows the diurnal and seasonal trend but with less daytime absorption. In both the observation and model the dawn and dusk terminator provide an unmistakable seasonal trend. For about two hours after sunset and before dawn, the observations show a transition region before reaching the nighttime signal level, but this feature is absent from the model results.

4.1.2. Signal at 5 MHz (Figure 9)

[27] The morphology is similar to the 2.5 MHz signal, propagating at night but absorbed during the day. The Klamath Falls measurements have *F* mode propagation throughout the night; however, the model shows occasional dropouts of the *F* mode propagation in the predawn hours. This discrepancy indicates that the IFM nighttime *F* region decays to peak values that are too low to refract the 5 MHz signal. Similar, but less dramatic, predawn dropouts may be seen in the observations (Figure 9, left) for example on 1 and 12 May and 18–20 September 2003. Modeled signal strength shows appropriate diurnal and seasonal trends but with too little absorption when compared with data.

[28] It should be noted that at BLO, the 5 MHz signal propagates around dawn and dusk when the *E* and *F* regions are dense but absorption is minimal; the *F* region is not dense enough late at night to refract the high-angle ray, and absorption attenuates the daytime signal. These data are not presented here but may be viewed online at http://www.spacenv.com/~rice/hidive.

4.1.3. Signal at 10 MHz (Figure 10)

[29] The diurnal behavior at 10 MHz changes, with the nighttime *F* region too weak to refract even the low-angle ray to Klamath Falls. Daytime absorption is less at this higher frequency, allowing the signals refracted by the strong daytime *E* and *F* regions to pass with less attenuation. The model captures the seasonal and diurnal climatology very well. Even the post sunset decay of the *F* region
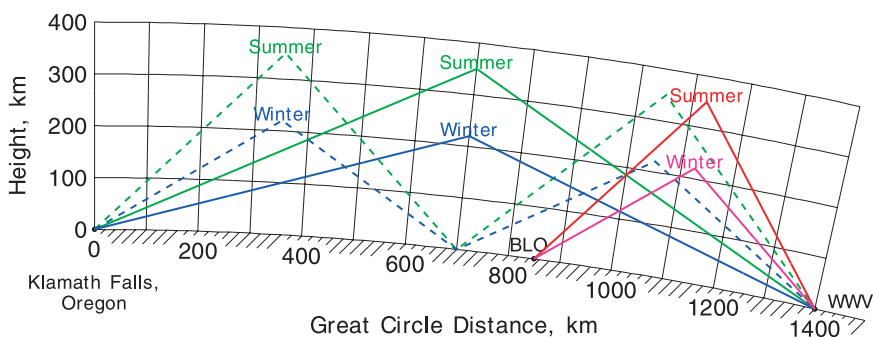
Figure 7. Vertical plane geometry for *F* region modes from WWV to Klamath Falls, summer and winter conditions.
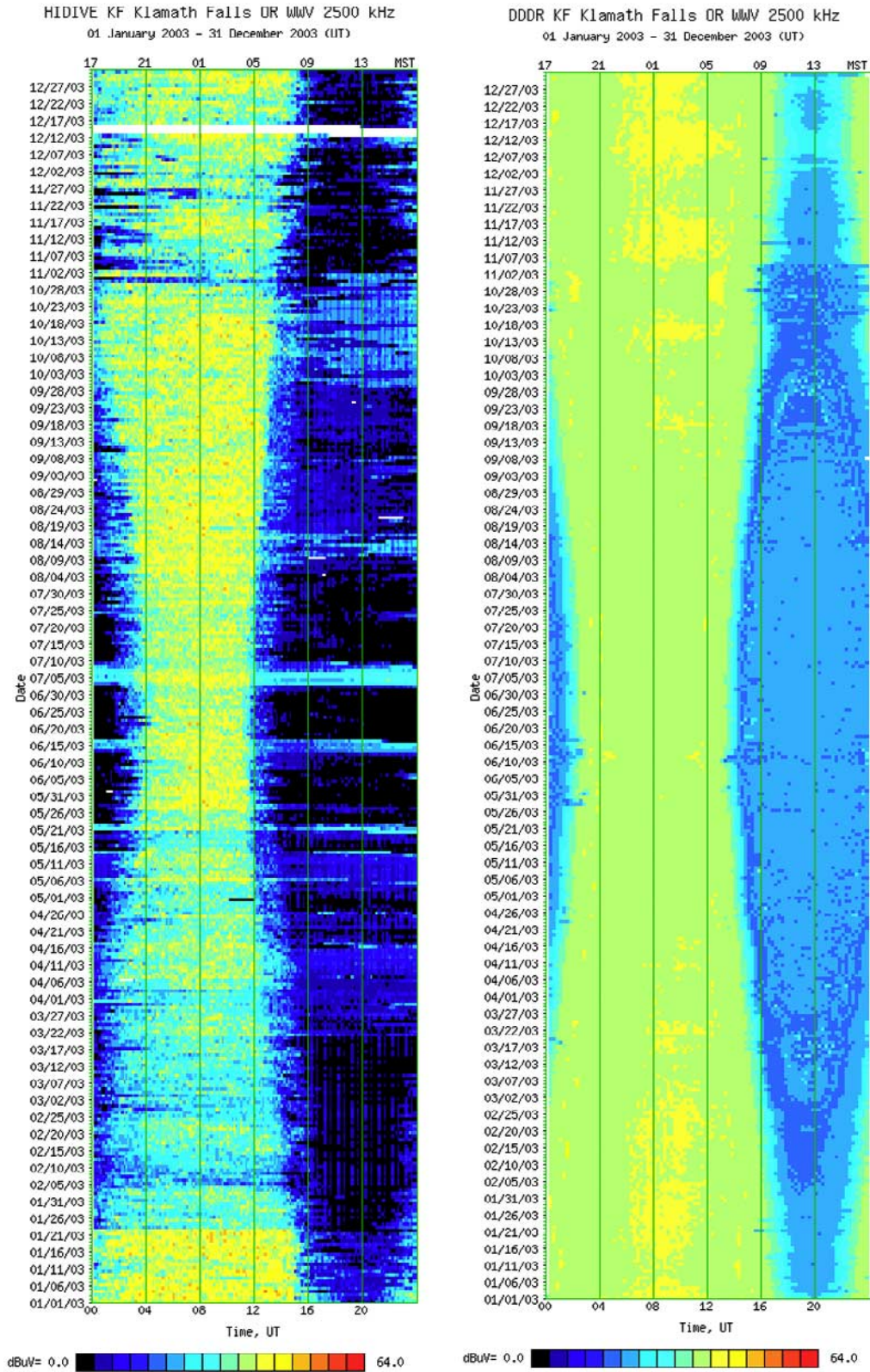
Figure 8. (left) WWV signal observed in Klamath Falls, Oregon, and (right) model signal strength for 2.5 MHz. Local time axis at path midpoint is shown along the top.
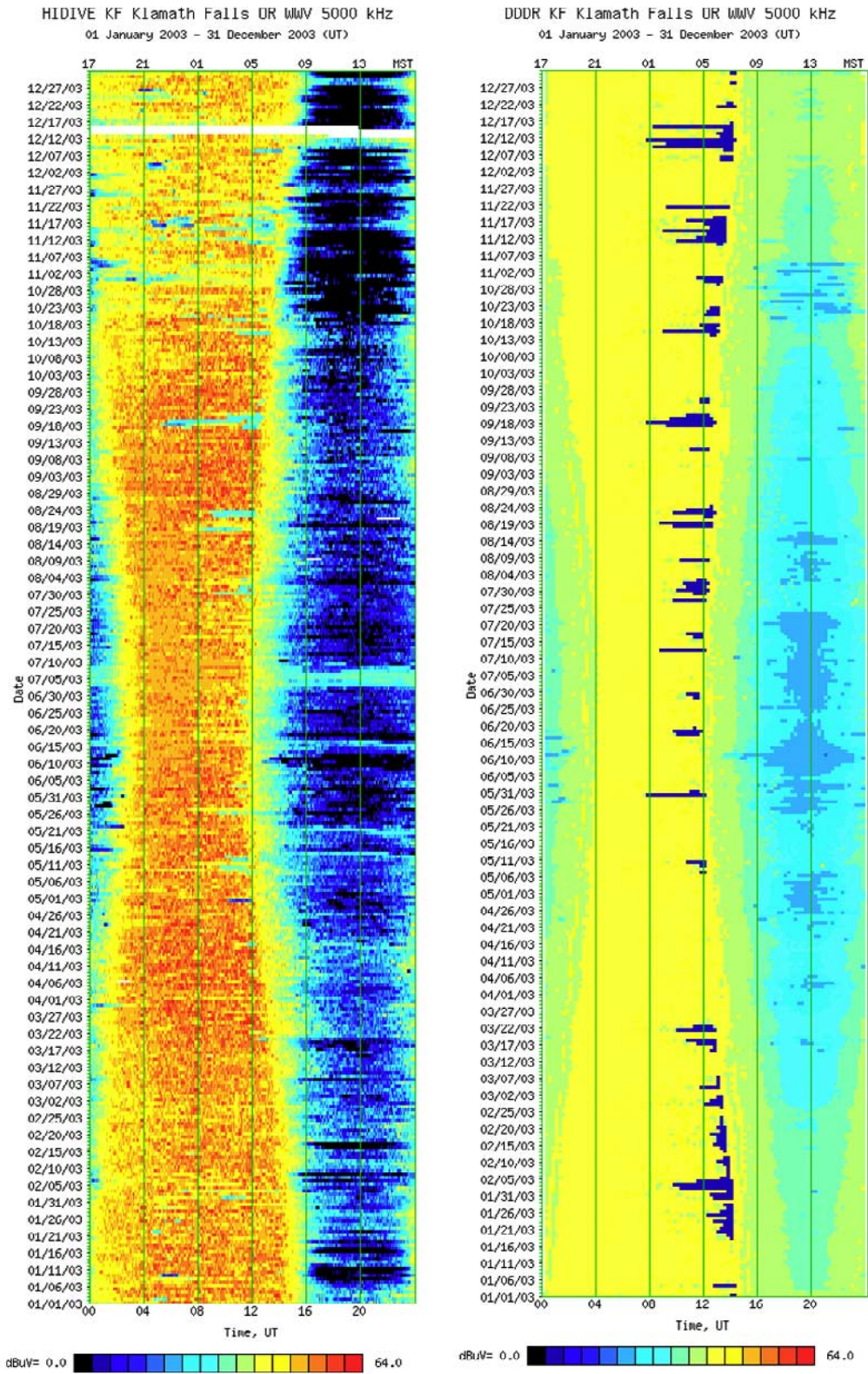
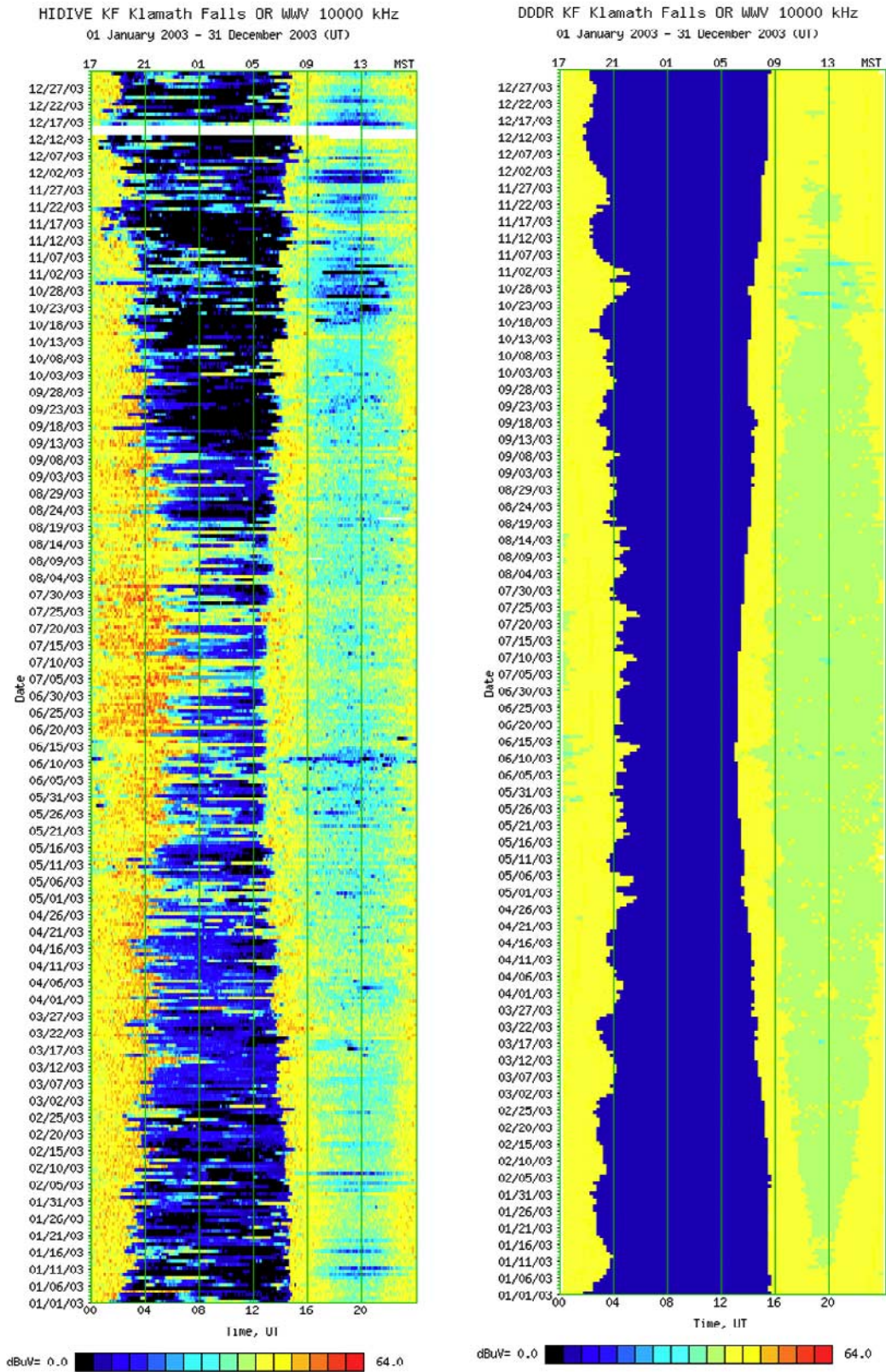**Figure 9.** (left) WWV signal observed in Klamath Falls, Oregon, and (right) model signal strength for 5 MHz.

ECCLES ET AL.: DATA-DRIVEN *D* REGION MODEL

Figure 10. (left) WWV signal observed in Klamath Falls, Oregon, and (right) model signal strength for 10 MHz.
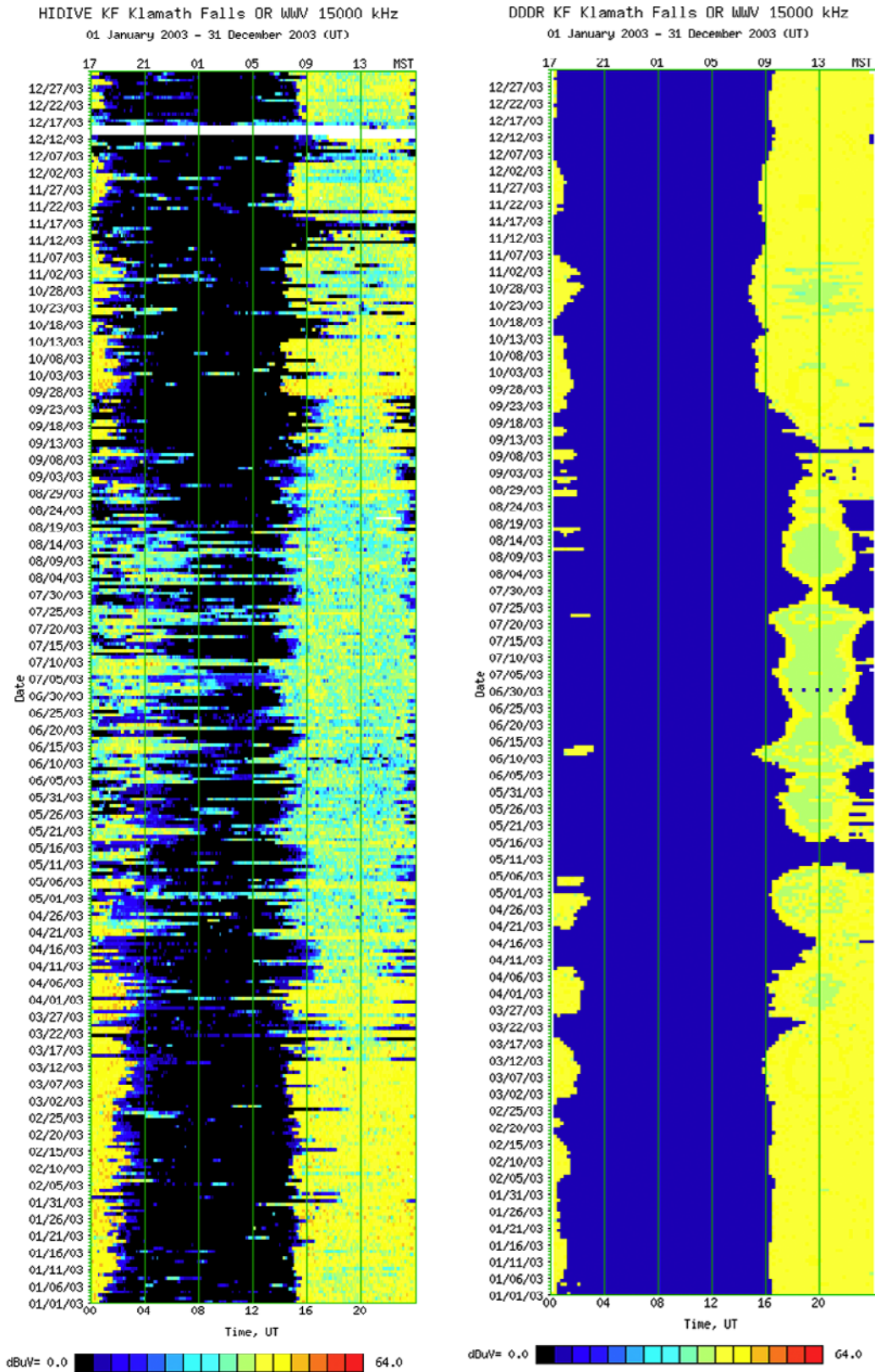
Figure 11. (left) WWV signal observed in Klamath Falls, Oregon, and (right) model signal strength for 15 MHz.

density captures solar rotation variations of the F10.7 values. This behavior is readily seen as the yellow-blue transition at about 0400 UT throughout the year. In the model this is a clean transition; the observations show a similar trend masked by weather variability but which nonetheless correlates with the 27-day F10.7 variation seen in the model.

4.1.4. Signal at 15 MHz (Figure 11)

[30] This higher frequency shows a seasonal behavior, changing near spring and autumn equinox. The model provides the reason for the seasonal change: in the winter, propagation is due to a relatively stable path via the daytime *F* layer; in the summer the dominant path shifts between the higher-altitude summer *F* layer and the daytime *E* layer as critical frequencies change during the day. The model also indicates the strong role of the solar rotation control of the solar EUV spectrum that modulates the *E* region in the summer daytime.

4.1.5. Signal at 20 MHz (Not Shown)

[31] This frequency is close to the MUF for the WWV-KF path, so propagation is very irregular and in the summer is often due to refraction from sporadic *E*. The model results suggest that the IFM *F* region ionosphere is a little too low in peak density, since it predicts no propagation at all on this path.

4.2. Weather Comparisons

[32] Weather effects, particularly those related to the *D* region, are of primary interest in this project. The observational data for 2003 show numerous weather effects, while the model demonstrates a subset of weather-related phenomena. The major classes of weather events are summarized below.

4.2.1. Winter Absorption Anomaly

[33] The winter anomaly [*Hargreaves*, 1992; *Davies*, 1990] has two facets:

[34] 1. HF absorption is generally greater in the winter by about a factor of 2 [3 dB] than one would predict by extrapolating summer measurements.

[35] 2. Absorption shows much greater variation in the winter and groups of days show levels of absorption that are abnormally high compared to the already high winter level; however, on some days absorption is low, comparable to summer days.

[36] This behavior can be seen in the daytime data for the 2.5–10 MHz frequencies; note the dark horizontal features on some winter (November–February) days for these frequencies (e.g., 9–12 January and 3–8 February in Figures 9 and 10). The features often appear to be correlated with the Utah data as well; for stations 800 km apart, *Schwentek* [1974] found the correlation coefficient to be about 0.4, so testing the correlation will be of interest as the data set grows. The model can reproduce absorption variations similar to those of the winter anomaly if NO is allowed to vary. *Hargreaves* [1992], summarizing the work on this subject, cites NO (possibly transported from high latitudes) as a potential driver for the winter anomaly. It is thus plausible that the model may be able to use the observed absorption to adjust its *D* region chemistry,

though the ramifications of this approach need to be explored in much greater detail.

4.2.2. X-Ray Flares

[37] The "Halloween storm" in late October through early November 2003 is clearly visible in the observed data, though effects during this period are complicated by massive flows of charged particles. Smaller flare effects may be observed in late March 2003, and late May through early June 2003. X-ray flare absorption has a characteristic sharp onset with gradual reduction to pre-flare levels over 20–60 min in the observed signals. The model which uses GOES X-ray measurements responds to X-ray flares with increased absorption. The estimated signal strength at the receiving site is strongly dependent on the ray paths in these cases: low-angle rays which travel long distances through the *D* and lower *E* regions will be strongly absorbed, while high-angle rays will suffer much less attenuation. This elevation angle dependence must be coupled to the frequency-dependent radiation pattern of the antenna. An X-ray flare response will be examined in more detail in the next section.

4.2.3. Sporadic *E*

[38] These layers were observed by the BLO ionosonde frequently throughout the summer, and irregularly through the rest of the year. Sporadic *E* refraction gives rise to abnormally high nighttime signal levels on the frequencies of 10 MHz and above; see Figures 10 and 11. Certain sporadic *E* geometries may also cause signal dropouts when the layer blocks a dominant *F* region ray path. The signal observations show sporadic signal enhancements, particularly during the summer, many corresponding to ionosonde sporadic *E* observations. For example, in Figure 10 the July 10 MHz observations show strong signal strengths through most of the night for at least six nights. The model does not attempt to include sporadic *E* physics, so this is another behavior for which observational data can supplement the model calculations to give a more complete and realistic picture of current conditions.

4.2.4. F10.7 Modulation

[39] The wave-like variations in the observed dusk propagation boundaries at 10 and 15 MHz correspond to changes in the solar F10.7 flux, which affects the *F* layer density. The period of the variation in the observed data is about 28 days, corresponding to the solar rotation period. These variations are reasonably well reproduced by the model.

5. X-Ray Flare Study

[40] The HIDIVE data set includes a large number of examples of X-ray flares. For modeling purposes, we wish to find a moderate daytime X-ray flare occurring in geomagnetically quiet conditions to reduce complications from other effects. One such example occurs on 26 February 2004, when two M-class flares occurred between 2000–2300 UT (local afternoon) and produced well-defined absorption in the HF signal data. The GOES 12 0.1 to 0.8 nm X-ray flux for this period is shown in Figure 12;

GOES 12 0.1-0.8 nm X-Ray Flux
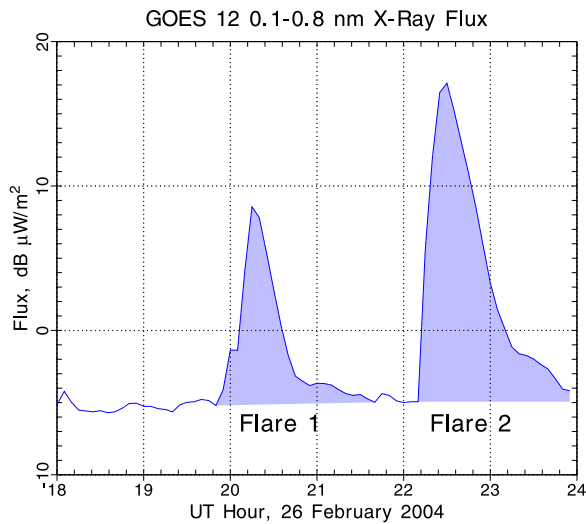
Figure 12. GOES 12 X ray in the 0.1−0.8 nm band on 26 February 2004. The two flares occurred during local afternoon on the WWV−to−Klamath Falls path.

the two flares have been shaded and labeled "flare 1" and "flare 2."

[41] The WWV signal strength at four frequencies observed in Klamath Falls is shown in Figure 13. The 2.5 MHz signal is already strongly attenuated by normal daytime absorption, so little flare effect can be seen at this frequency. The 5 MHz signal is also attenuated, but it fades to the noise floor as a result of the flares. The 10 and 15 MHz signals suffer the least daytime absorption, and show well-defined flare signatures. For both flares the response in the signal strength begins at the initial rise of the flare and peaks at the time of the flares' peaks, indicating an immediate ionospheric response to the energetic solar photons.
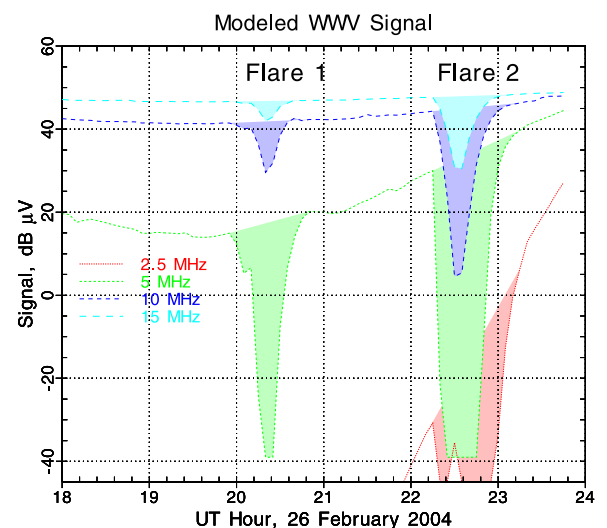
[42] The model response at the same four frequencies is shown in Figure 14. The 2.5 MHz signal is attenuated well below the noise floor by normal daytime absorption, as seen in the observational data. The 5 MHz signal is completely absorbed as a result of both X-ray flares, even given the greater dynamic range of the simulated signal compared to the observed signal. The 10 and 15 MHz signals show well-defined flare responses, as observed. The modeled flare responses follow the observed signal responses, which have been shown to track the GOES measurements of high-energy photons in the flare. At 10 MHz for flare 1 the modeled maximum change in signal strength is 12 dB while the observed value is 18 dB. For flare 2 the model change is 42 dB while the observed value is slightly larger than 32 dB. Only flare 2 can be compared at 15 MHz; the model value is 17 dB while the observed value is 21 dB.

[43] A further validation of the DDDR model to predict the KF signal strength from the WWV transmitter is the need for the flare ionization impact to have an inverse frequency-squared dependence. Flare 1 (Figure 14) has model responses at 5, 10, and 15 MHz that can be inferred

Klamath Falls WWV Signal
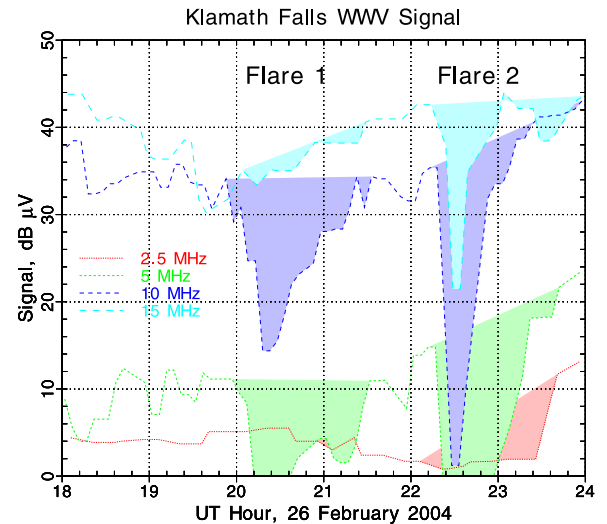
Figure 13. WWV signal strength observed in Klamath Falls from 1800 to 2400 UT on 26 February 2004. The responses to the two X-ray flares on four frequencies are shown as the color-shaded areas.

above background or noise floor. The maximum signal strength changes are about 60 dB, 12 dB, and 4.0 dB at 5, 10, and 15 MHz respectively. The inverse frequency-squared relationship if normalized to 60 at 5 MHz predicts the 5:10:15 MHz ratios as 60:15:6.7. The model ratios of 60:12:4.0 compare favorably with this scaling law. Issues associated with frequency dependence of antenna patterns

Modeled WWV Signal

Figure 14. DDDR-modeled signal strength for WWV−to−Klamath Falls path at the same four frequencies shown in Figure 13. The color scheme and shading are the same as used to represent flare responses in Figure 13.

have as yet not been folded into the DDDR model calculations. This matter is discussed further in the next section.

6. Summary

[44] Using continuously recorded HF signal amplitudes from WWV supplemented with selected space weather information, we are developing a data source suitable for near-real-time assimilation for ionospheric and propagation specification and forecast models. The observed HF amplitude fading reflects weather events such as solar X-ray flare and winter anomaly absorption, while HF amplitude enhancements indicate propagation paths being facilitated by effects such as sporadic *E* layers or combined *E* and *F* layers. The HF digital monitoring system described here is unique and inexpensive, providing continuous (1-min averaged) signal amplitude variation data at 2.5, 5.0, 10.0, 15.0 and 20.0 MHz. Data have been collected since December 2002, and the data obtained for this project should cover the declining phase of solar cycle 23 (December 2002 through June 2005.) This period has already included very large geomagnetic and solar radiation storms and should see a decrease in 10.7 cm solar flux by a factor of more than 2. Although we are monitoring signals from WWV and WWVH at several sites, we have concentrated our initial analysis on the midlatitude path from WWV (Ft. Collins, Colorado) to Klamath Falls, Oregon; as the analysis matures, the other paths in the data set will be examined.

[45] The Data-Driven *D* Region (DDDR) model has been developed as a first step in calculating *D* region absorption at midlatitudes. This model is extended upward through the *E* and *F* region using the Ionospheric Forecast Model (IFM.) Together this complement of models provides a full description of the plasma medium through which the HF signals propagate. To analyze propagation, an HF ray-tracing code HASEL [*Coleman*, 1993] determines the *E* and *F* region paths as well as multihop paths between the selected transmitter and receiver. The absorption calculations include full path calculations through the *D*, *E*, and *F* regions restricted to nondeviative absorption, and include focusing effects. At this time frequency dependencies and angle of arrival of rays at the antennas have not be folded into the calculations.

[46] In this study results have been presented from the data collection system (HIDIVE) and separately from the model (DDDR.) These two aspects are to be merged such that the model can be data driven from observations; current efforts are aimed at developing an assimilation technique to provide near-real-time specification. That the DDDR modeling provides a reasonable first level representation of the HIDIVE observations (Figures 8–11) is a necessary first step for a successful assimilation model.

[47] The DDDR model is already data driven in that it requires indices F10.7, F10.7A, and *Kp* as well as GOES X-ray fluxes. Two possible assimilation objectives are being studied: detecting the presence of sporadic *E* layers that are readily identified in the HF signal strength data

but are not included in the physics of DDDR; and secondly using the variable daytime HF fades found in winter, probably reflecting NO density changes, to improve specification of the NO density distribution at midlatitudes in the model. Neither of these phenomena is homogeneous over a continental scale and hence the HIDIVE network would need to be extended in order for the assimilation process to have a knowledge of these inhomogeneities.

[48] One could envision a network of HF monitors supplying data to an integrated ionospheric physics/ray tracing model to provide complete ionospheric specification and propagation ''nowcasting'' for scientists and HF communicators. Such a system would require regional beacons to provide short one-hop signal paths, rather than relying on broadcasters like WWV/WWVH with paths that may involve multiple hops. But what spacing would be needed to study *D* region absorption variations?

[49] *Schwentek* [1974] found that changes in midlatitude absorption were well correlated for stations within about 200 km of each other, but correlation decreased rapidly as spacing increased to 500 km. For spacing between 500–1000 km, correlation was relatively constant at about 0.4. Observational spacing in the 200–500 km range would thus allow mapping of absorption variations without excessive duplication. This spacing is consistent with the Distributed Array of Small Instruments (DASI) midlatitude ground-based network proposed by *Sojka et al.* [2004]. Our project will continue to investigate the feasibility of such a system and will work toward data-driven assimilation modeling that will more faithfully reproduce the effects of space weather on the ionosphere and HF propagation through it.

References

American Radio Relay League (2003), *ARRL Antenna Book*, 20th ed., Newington, Conn.

Anderson, G. P., S. A. Clough, F. X. Kneizys, J. H. Chetwynd, and E. P. Shettle (1986), AFGL atmospheric constituent profiles (0–120 km), *Rep. AFGL-TR-86–0110*, Air Force Geophys. Lab., Hanscom AFB, Mass.

Banks, P. M., and G. Kockarts (1973), *Aeronomy*, Academic, San Diego, Calif.

Bishop, G., T. Bullett, K. Groves, S. Quigley, P. Doherty, E. Sexton, K. Scro, R. Wilkes, and P. Citrone (2004), Operational Space Environment Network Display (OpSEND), *Radio Sci.*, *39*, RS1S26, doi:10.1029/2002RS002836.

Bixby, L. H., Jr. (1956), Interpretation of WWV and WWVH signal strength variations at Stanford, Ph.D. dissertation, Stanford Univ., Stanford, Calif.

Coleman, C. J. (1993), A general purpose ionospheric ray tracing procedure, *Rep. SRL0131TR*, Def. Sci. and Technol. Org., Adelaide, S. A., Australia.

Cook, S. C. (1997), HF communications in the information age, paper presented at 7th International Conference on HF Radio Systems and Techniques, Inst. of Electr. Eng., Stevenage, U. K.

Croft, T. A. (1972), Sky-wave backscatter: A means for observing our environment at great distances, *Rev. Geophys.*, *10*, 73–155.

Davies, K. (1990), *Ionospheric Radio*, Peter Peregrinus, London.

Goodman, J. M. (1992), *HF Communication: Science and Technology*, Van Nostrand Reinhold, New York.

Hargreaves, J. K. (1992), *The Solar-Terrestrial Environment*, Cambridge Univ. Press, New York.

Hedin, A. E. (1991), Extension of the MSIS thermosphere model into the middle and lower atmosphere, *J. Geophys. Res.*, *96*, 1159–1172.

Hindmarsh, A. C. (1983), Odepack, a systematized collection of ode solvers, in *Scientific Computing*, edited by R. S. Stepleman et al., pp. 55–64, North-Holland, New York.

Hunsucker, R. D. (1991), *Radio Techniques for Probing the Terrestrial Ionosphere*, Phys. Chem. Space Ser., vol. 22, Springer-Verlag, New York.

Hunsucker, R. D., and J. K. Hargreaves (2003), *The High-Latitude Ionosphere and its Effects on Radio Propagation*, Cambridge Atmos. Space Sci. Ser., Cambridge Univ. Press, New York.

Kirby, K., E. R. Constantinides, S. Babeu, M. Oppenheimer, and G. A. Victor (1979), Photoionization and photoabsorption cross sections of He, O, N_2, and O_2 for aeronomic calculations, *At. Data Nucl. Data Tables*, *23*, 63–81.

Lanzerotti, L. J. (2001), Space weather effects on technologies, in *Space Weather*, Geophys. Monogr. Ser., vol. *125*, edited by P. Song, H. J. Singer, and G. L. Siscoe, pp. 11–22, AGU, Washington, D. C.

McNamara, L. F. (1991), *The Ionosphere: Communications, Surveillance and Direction Finding*, Krieger, Melbourne, Fla.

Murtagh, W., L. Combs, and J. Kunches (2004), A workshop for the aviation community, *Space Weather*, *2*, S06004, doi:10.1029/2004SW000081.

Renfree, P. (2001), The US Navy returns to HF with STANAG 5066 as the path, in *Milcom 2001 Proceedings: Communications for Network-Centric Operations: Creating the Information Force, 28–31 October 2001, Tysons Corner, McLean, Virginia USA*, vol. 1, pp. 471–476, IEEE Press, Piscataway, N. J.

Richards, P. G., J. A. Fennelly, and D. G. Torr (1994a), EUVAC: A solar EUV flux model for aeronomic calculations, *J. Geophys. Res.*, *99*, 8981–8992.

Richards, P. G., J. A. Fennelly, and D. G. Torr (1994b), Correction to "EUVAC: A solar EUV flux model for aeronomic calculations," *J. Geophys. Res.*, *99*, 13,283–13,284.

Schunk, R. W., J. J. Sojka, and J. V. Eccles (1997), Expanded capabilities for the ionospheric forecast model, *Rep. AFRL-VS-HA-TR-98–0001*, Space Vehicles Dir., Air Force Res. Lab., Hanscom AFB, Mass.

Schwentek, H. (1974), Some results obtained from the European Cooperation concerning studies of the winter anomaly in ionospheric absorption, in *Methods of Measurement and Results of Lower Ionosphere Structure*, edited by K. Rawer, pp. 293–303, Akademie, Berlin.

Sojka, J. J., D. Rice, J. V. Eccles, F. T. Berkey, P. Kintner, and W. Denig (2004), Understanding midlatitude space weather: Storm impacts observed at Bear Lake Observatory on 31 March 2001, *Space Weather*, *2*, S10006, doi:10.1029/2004SW000086.

Strobel, D. F., C. B. Opal, and R. R. Meier (1980), Photoionization rates in the night-time *E*- and *F*-region ionosphere, *Planet. Space Sci.*, *28*, 1027–1033.

————————————

J. V. Eccles, D. Rice, and J. J. Sojka, Space Environment Corporation, 221 N Spring Creek Parkway, Providence, UT 84332, USA. (vince.eccles@spacenv.com)

R. D. Hunsucker, RP Consultants, 7917 Gearhart, Klamath Falls, OR 97601, USA.